The Effect of Solute Content on the Slip Behavior in 7XXX Series Aluminum Alloys

GERARD M. LUDTKA AND DAVID E. LAUGHLIN

The microstructures of three high strength, high purity Al-Zn-Mg-Cu alloys, in the T6 temper, were characterized extensively using quantitative optical metallography and quantitative transmission electron microscopy. Only the solute content (Mg + Zn) of these alloys was varied for this study. These alloys were shown to be identical in grain size and shape, dispersoid (E-phase) and grain boundary precipitate (η) populations, and precipitate free zone widths. The matrix microstructures consisted of ordered GP zones and η' and differed only in the volume fraction of these strengthening precipitates. The higher solute alloys had the higher yield strengths and volume fractions of matrix precipitates. Subsequent slip behavior analysis of prestrained tensile specimens demonstrated that slip band spacings and slip step heights increased with increasing solute content for the same macroscopic strain ($\epsilon_p = 0.02$). A work softening model by Hornbogen and Gahr was shown to predict this tendency toward increased strain localization with higher solute levels.

IN the field of materials, there is a continual search for stronger alloys. The increase of resistance to plastic deformation of metallic structures permits the design and construction of structures which perform the desired function using less material. This is an especially important consideration in the area of transportation since lighter vehicles would be more energy efficient. One method of increasing strength is precipitation strengthening. Many alloy systems are amenable to this approach and the influence of the strengthening precipitates on slip behavior has been the topic of many investigations, *e.g.*, Gysler, Lutjering and Gerold[1] for Ti-Mo; Lutjering and Weisman,[2] and Blackburn and Williams[3] for Ti-Al; Price and Kelly[4] for Al-Ag and Al-Zn; Evensen, Ryum, and Embury,[5] for Al-Mg-Si; and Hornbogen and Gahr,[6] for Fe-Ni-Al. Nock and Hunsicker[7] have demonstrated that the maximum attainable yield strength in the 7XXX series alloys (Al-Zn-Mg-Cu-Cr) can be extended from 517 MPa to 690 MPa by increasing the solute (Mg and Zn) content. However, these ultra high strength alloys have very low fracture toughness values. The mechanisms responsible for this loss of toughness with increasing solute content have not been defined.

The purpose of this investigation was to evaluate the influence of the volume fraction of strengthening precipitate on the matrix slip behavior of three ultra high purity, ultra high strength 7XXX series aluminum alloys in the T6 temper. This characterization will provide information necessary to understand the response of these alloys to macroscopic strains. Subsequent research[8] has utilized the findings of this study to explain the loss of fracture toughness with increasing yield strength and concomitant transition in fracture mode observed.

GERARD M. LUDTKA, formerly a Research Assistant at Carnegie-Mellon University, is now Senior Research Engineer, General Motors Research Laboratories, Warren, MI 48090. DAVID E. LAUGHLIN is Associate Professor, Metallurgical Engineering and Material Science Department, Carnegie-Mellon University, Pittsburgh, PA 15213.

Manuscript submitted April 2, 1981.

MATERIALS AND PROCESSING

Composition

Three different compositions were selected to provide a spectrum of yield strength values and volume fractions of strengthening precipitates (Table I). These alloys differ from one another only in Mg and Zn contents. A ratio of Mg to Zn between 0.35 to 0.40 was maintained for this study. The normal additions found in the 7XXX series aluminum alloys (Cu, Cr, Ti, B, Be) were added so that comparisons of properties with commercial alloys would be possible. In order to make an accurate evaluation of the effect of the strengthening precipitate, high purity base aluminum and alloying additions were used so that the large (0.1 to 30 μm) Fe and Si and bearing constituents generally present in commercial 7075 in amounts ranging from 1 to 5 vol pct could be precluded. The Fe and Si contents were each less than 0.01 wt pct in the final alloys.

A high purity version of a commercial 7075 composition was chosen as one of the three alloys. This serves as a reference whereby the normal yield strength level of approximately 504 MPa in the T6 temper is obtained. The 7075 aluminum alloy has 2.20 wt pct Mg and 5.59 wt pct Zn. This lowest Mg + Zn alloy will be referred to hereafter as the *low solute* alloy. The other two alloys have increasingly higher Mg and Zn contents and provide substantial increases in yield strength of 87 MPa and 118 MPa. These compositions will be referred to as the *intermediate solute* (2.81 wt pct Mg-6.96 wt pct Zn) and *high solute* (2.76 wt pct Mg-7.84 wt pct Zn) alloys in subsequent discussions.

Processing

All three alloys were produced and processed in an identical manner. These were cast into 15.2 × 40.6 × 91.4 cm ingots and subsequently scalped down to 14 cm thick to remove surface scale and defects. They were preheated to 471 °C for 24 h in a fluoborate atmosphere prior to fabrication into 1.6 mm thick sheet. The sheet

ISSN 0360-2133/81/1211-2083$00.75/0
 © 1981 AMERICAN SOCIETY FOR METALS AND THE METALLURGICAL SOCIETY OF AIME

Table I. Chemical Composition Analysis (Wt Pct)

Alloy Designation	Mg	Zn	Cu	Cr	Si	Fe	Ti
Low solute	2.20	5.59	1.54	0.19	0.009	0.007	0.02
Intermediate solute	2.81	6.96	1.56	0.19	0.010	0.009	0.02
High solute	2.76	7.84	1.55	0.19	0.008	0.020	0.01

Note: Mn, Ni, B $<$ 0.01; Be $<$ 0.001.

processing involved hot rolling at 427 °C (800 °F) to 25.4 mm, reheating in the fluoborate atmosphere for 48 h at 471 °C, hot rolling at 427 °C to 6.4 mm, and finally cold rolling to the final 1.6 mm dimension. At no time were these cross rolled, or hot rolled below 371 °C.

Heat Treatment

For this study only the T6 temper was investigated for the sheet material. All of the alloys were solution treated for one hour at 471 °C and cold water quenched from the solution temperature. They were stretched 1 to 3 pct to flatten, and finally aged fo 24 h at 121 °C.

EXPERIMENTAL PROCEDURE

The microstructures of the various alloys were examined using optical microscopy. Metallographic preparation involved normal procedures of using a series of abrasive papers, diamond pastes, and a final polishing with a slurry made of reagent grade MgO and distilled water. At this point, all of the Fe and Si based constituents were clearly visible in the microscope and their volume fraction determinations could be made without etching. To show the grain boundary morphology, the specimens were etched by immersion into Keller's etchant.[9]

Constituent volume fraction measurements were made at a magnification of 500 times using a grid containing 696 points. Thirty random views on each of five specimens per alloy were examined. The locations of the constituents within each alloy were assumed to be random, therefore, the volume fraction, V_v, is given by $\overline{P}_p$ (Ref. 10) which is the fraction of total grid points that fall on constituent particles. Constituents smaller than 0.1 μm were not measured.

Intercept grain sizes in three orthogonal directions were measured to characterize the grain morphology. The technique employed is described in detail by Schuckher.[11] Mean values and standard deviations for the intercept grain sizes were determined on the basis of three separate measurements on each of five different specimens per alloy per direction. Thin foils for microstructural characterizations in the TEM were made using a 1/3 nitric-2/3 methanol solution in a Fischione fiber optic, twin jet electropolishing unit.[12] After thinning, the specimens were rinsed twice in methanol, dried, and examined immediately in a JEOL Ltd. JEM 100B transmission electron microscope at 100 KV.

Quantitative transmission electron microscopy was performed to characterize the matrix Cr-dispersoid (E-phase) and grain boundary $MgZn_2$ (η) precipitate populations for each alloy, and to determine precipitate free zone (PFZ) widths. For the Cr-dispersoids, average diameters, $\overline{d}_D$, interparticle spacings, $\overline{\lambda}_D$, particle densities, $\overline{N}_v$, and volume fractions were determined. Since the Cr-dispersoids are irregular in shape, an effective particle diameter, d_e, was defined as:

$$d_e = \sqrt{d_1 d_2} \quad [1]$$

where d_1 and d_2 are the smallest and largest dimensions of a dispersoid, respectively. The average effective dispersoid diameter, $\overline{d}_D$, of n particles is given by:

$$\overline{d}_D = \frac{\sum_{i=1}^{n} \sqrt{d_{1i} d_{2i}}}{n} \quad [2]$$

To obtain the value of $\overline{d}_D$ for each alloy, at least 50 dispersoids were measured in each of eight different thin foils.

The interparticle spacings, $\overline{\lambda}_D$, is given by:[13]

$$\overline{\lambda}_D = \frac{0.554}{(\overline{N}_v)^{1/3}} \quad [3]$$

and the volume fractions of dispersoids by:

$$\text{volume fraction} = \frac{(\pi \overline{d}_D^3)}{6} \overline{N}_v \quad [4]$$

The particle density $\overline{N}_v$ is defined as:[14]

$$\overline{N}_v = \frac{N_A}{(t + \overline{d}_D)} \quad [5]$$

where t is the foil thickness and is easily obtained as described in Ref. 15 utilizing a grain boundary fringe technique. N_A is the number of dispersoids per unit area of projected image.

The grain boundary precipitates were characterized by calculating precipitate diameters, $\overline{d}_p$, intraplanar spacings, $\overline{\lambda}_p$, numbers per unit area, $\overline{N}_A$, and areal fractions, $\overline{f}_p$. This was accomplished using a parallax technique[16,17] on tilted grain boundaries. Initially stereo pair micrographs were taken of a tilted grain boundary. The angle of tilt between stereo pairs was 10 deg. High angle grain boundaries were recorded and data were

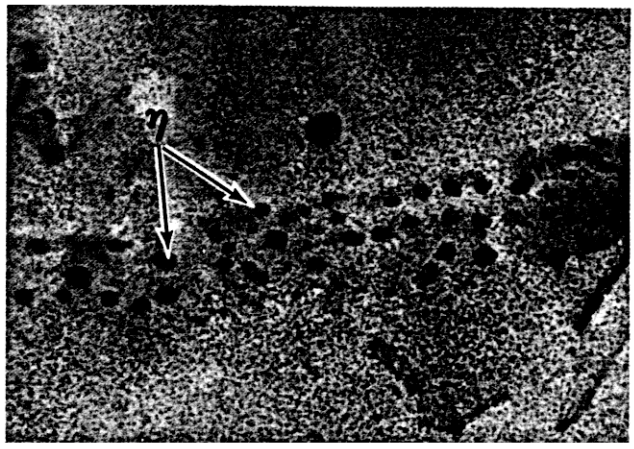

Fig. 1—Bright field TEM micrograph showing grain boundary η precipitates.

obtained on three sets of stereo pair micrographs per alloy. Figure 1 exhibits a typical tilted grain boundary showing the grain boundary precipitates.

The number of precipitates per unit area, $\overline{N}_A$, is given by:

$$\overline{N}_A = \frac{N}{A_{GB}} \quad [6]$$

where N is the number of precipitates counted on the projected grain boundary area, A_{GB}. The technique employed to calculate the projected grain boundary area is described elsewhere.[18] Using the relationship given by Gurland,[13] the average precipitate intraplanar spacing (average distance between nearest neighbors of point particles in a plane) is calculated from:

$$\bar{\lambda}_p = \frac{0.5}{\overline{N}_A^{1/2}} \quad [7]$$

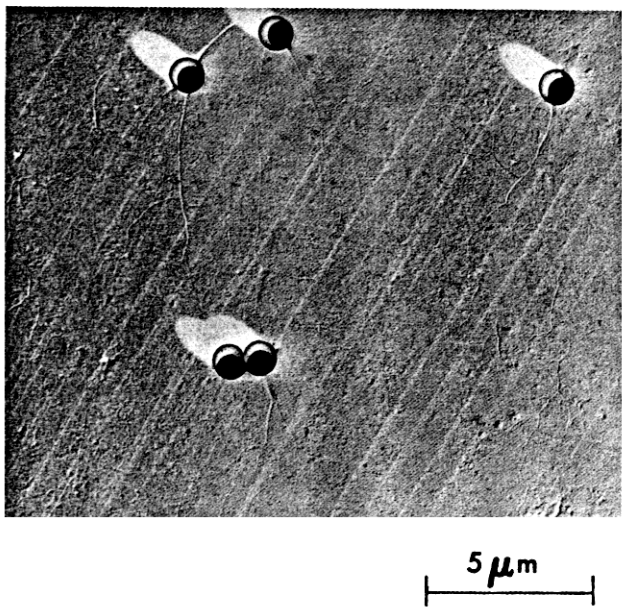

Fig. 2—Typical TEM micrograph of a replica for slip step height measurements.

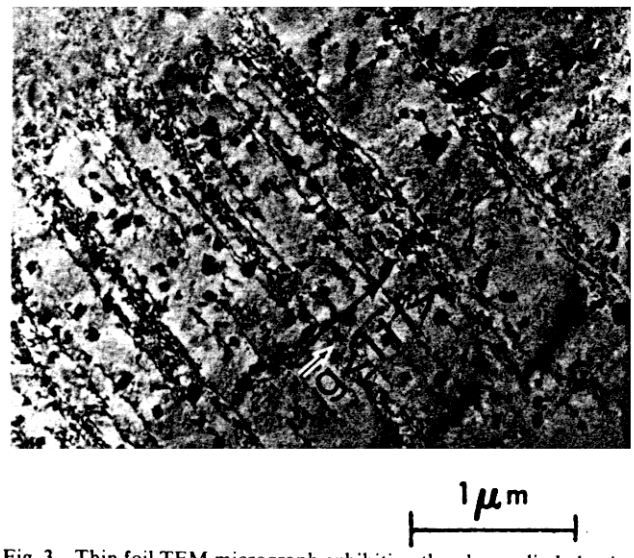

Fig. 3—Thin foil TEM micrograph exhibiting the planar slip behavior characteristic of all alloys (ϵ_p = 0.02).

The average precipitate diameters, $\overline{d}_p$, were determined by measuring all of the precipitates on the grain boundary. Areal fractions were estimated using the average values for $\overline{d}_p$ and $\overline{N}_A$.

Precipitate free zone (PFZ) widths were determined using the technique presented by Shastry and Judd.[19] Eight different grain boundaries per alloy were evaluated to obtain the means and standard deviations for the PFZ widths.

Tensile Property Determination

All of the tensile tests were performed using a 220 KN capacity MTS 810 Materials Test System at a strain rate of $4 \times 10^{-4}\ s^{-1}$. The procedure to determine the various data was that outlined in the ASTM E8-69 specification.[20] Sheet specimens with a 25.4 mm gage length and 6.4 mm width were used. Flow curve parameters for two different curve fit forms were determined subsequently using the least squares best fit curve fitting program of a HP-65 programmable calculator.

Slip Behavior Characterization

The slip behaviors of the alloys were characterized quantitatively from measurements made on prestrained tensile specimens (ϵ_p = 0.02). To obtain slip band spacings, thin foils were made from these specimens and viewed in the TEM. The foils were tilted until slip bands were visible and normal to an operating $\langle 1\bar{1}1 \rangle$ **g** vector. Under these conditions, the slip band spacings were determined.

Slip step heights were evaluated using latex spheres on platinum-carbon shadowed lucite replicas[21] made of the electropolished surfaces of the prestrained tensile specimens. A typical example of a replica showing the slip steps and latex spheres is presented in Fig. 2. A

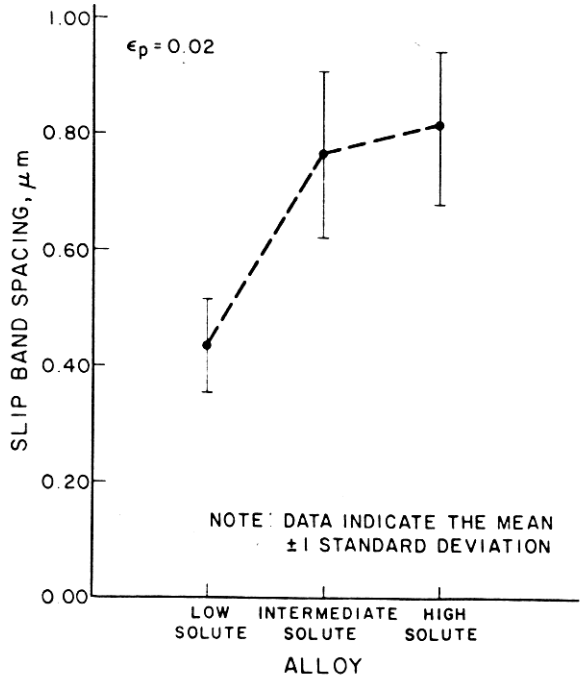

Fig. 4—Slip band spacings as a function of the solute content.

detailed discussion of the technique and equations used to determine the slip step heights is presented elsewhere.[18]

RESULTS AND DISCUSSION

The slip behaviors of these alloys were examined to detect any possible difference in their response to plastic deformation. For all of the alloys, the matrix slip was planar. Although distinct bands were seen they were somewhat diffuse (had some width) as is seen in Fig. 3. This is to be expected since the distribution of incoherent E-phase dispersoids tends to force the matrix to deform more homogeneously by inducing Orowan bowing of dislocations. At the same time, the fine strengthening precipitates promote heterogeneous deformation in the form of discrete slip bands. The competition between the two determines the final behavior of these alloys which is presented graphically in Fig. 4. The slip band spacings for the intermediate and high solute alloys are larger than those for the low solute alloy. In other words, at 2 pct strain, the slip is coarser in the higher solute alloys.

For constant macroscopic strain, if the slip bands are coarser in the higher solute alloys, then the slip step heights should be larger also. This indeed was seen to be the case when the low and high solute alloy slip step heights are compared (Fig. 5). Hence, for the same strain level, a conclusion can be made that the high solute alloy will have more strain localization, *e.g.*, at a slip band-grain boundary intersection, than the low solute alloy. Void formation at the grain boundary may result as is shown in Fig. 6(*b*) at a grain boundary dispersoid for the high solute alloy. Fracture of grain boundaries due to the intersections of slip bands with the boundary has been observed by Gysler, *et al.*,[1] in Ti-Mo alloy, by Lutjering and Weismann,[2] in Ti-Al alloys, and by Evensen, *et al.*,[5] in Al-Mg-Si alloys. This increasing tendency toward strain localization with increasing solute content can alter the response of the bulk material to macroscopic strains. In particular, the fracture toughness of these alloys has been shown to depend on this behavior.[8,18] Extensive microstructural characterizations were performed to facilitate a correlation between slip behavior and microstructure.

Metallographic examination revealed a fine grained recrystallized microstructure with a pancake shaped grain morphology as shown in Fig. 7. In the rolling plane, these grains appear almost equiaxed. For all compositions, the grains have average intercept grain dimensions of approximately 37 × 35 × 17 μm. Table

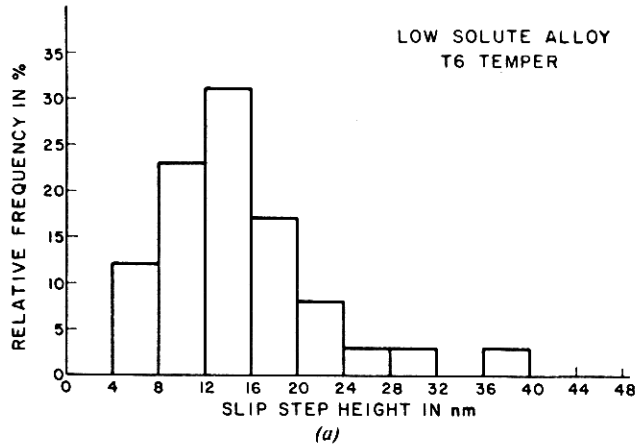

Fig. 5—Frequency diagrams of slip step heights for the (*a*) low, and (*b*) high solute alloys.

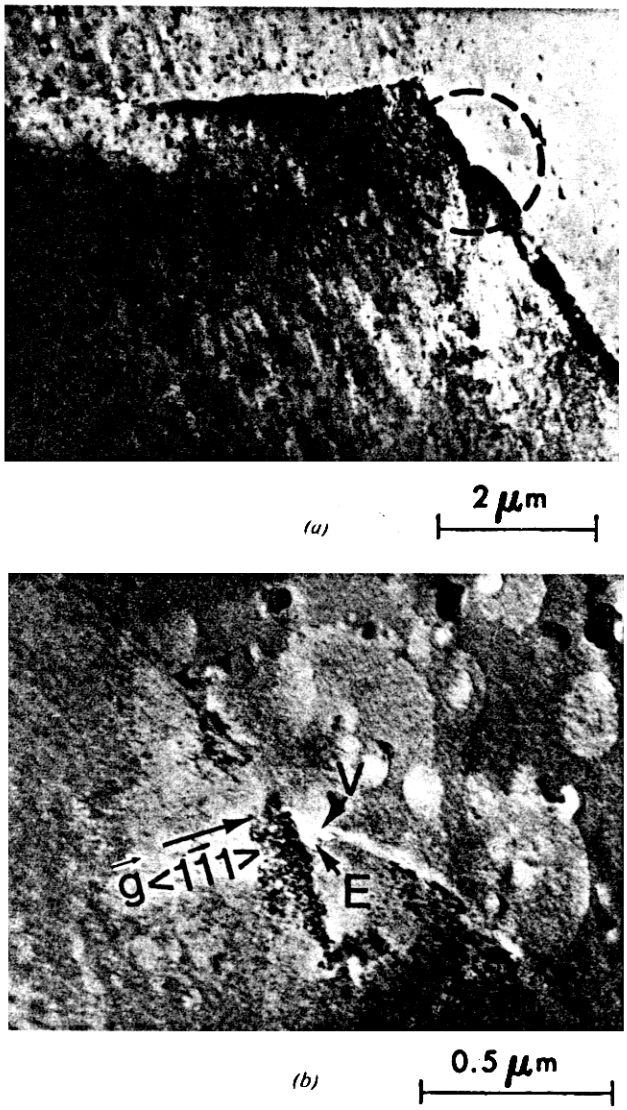

Fig. 6—(*a*) Bright field TEM micrograph from a prestrained tensile specimen of the high solute alloy at ϵ_p = 0.21; (*b*) Higher magnification view of encircled region in part (*a*) ("v"designates a void).

Table II. Intercept Grain Sizes*

Alloy	Longitudinal Direction† (μm)	Long Transverse Direction‡ (μm)	Short Transverse Direction¶ (μm)
Low solute	38.9 ± 2.3	35.0 ± 2.1	17.3 ± 0.6
Intermediate solute	35.3 ± 1.8	34.9 ± 1.5	16.4 ± 0.7
High solute	35.9 ± 3.8 (35.9 ± 3.8 for High Solute Alloy.)	34.6 ± 3.0	16.3 ± 0.7

*Data indicate the mean ± one standard deviation.
†Rolling direction.
‡In the rolling plane but perpendicular to the rolling direction.
¶Through the thickness direction.

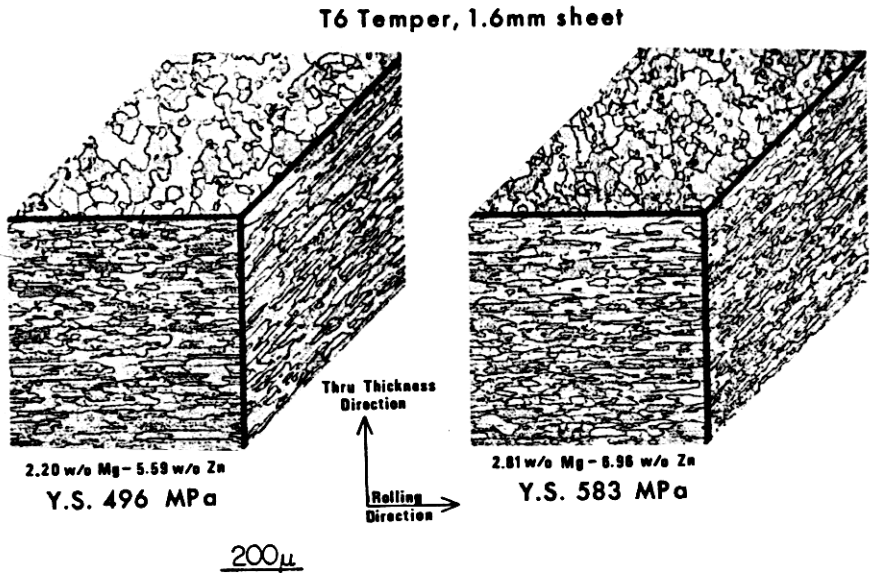

Fig. 7—Optical micrographs of the alloys investigated.

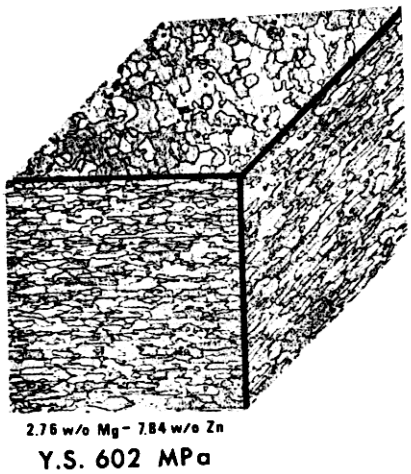

Table III. Fe- and Si-Bearing Constituent Vol Pct Data*

Alloy	Vol Pct of Constituents
Low solute	0.005 ± 0.010
Intermediate solute	0.011 ± 0.008
High solute	0.017 ± 0.014

*Data indicate the mean ± one standard deviation.

Table IV. Precipitate Free Zone (PFZ) Widths*

Alloy	PFZ Width, Å
Low solute	280 ± 29
Intermediate solute	269 ± 31
High solute	267 ± 31

*Data indicate the mean ± one standard deviation.

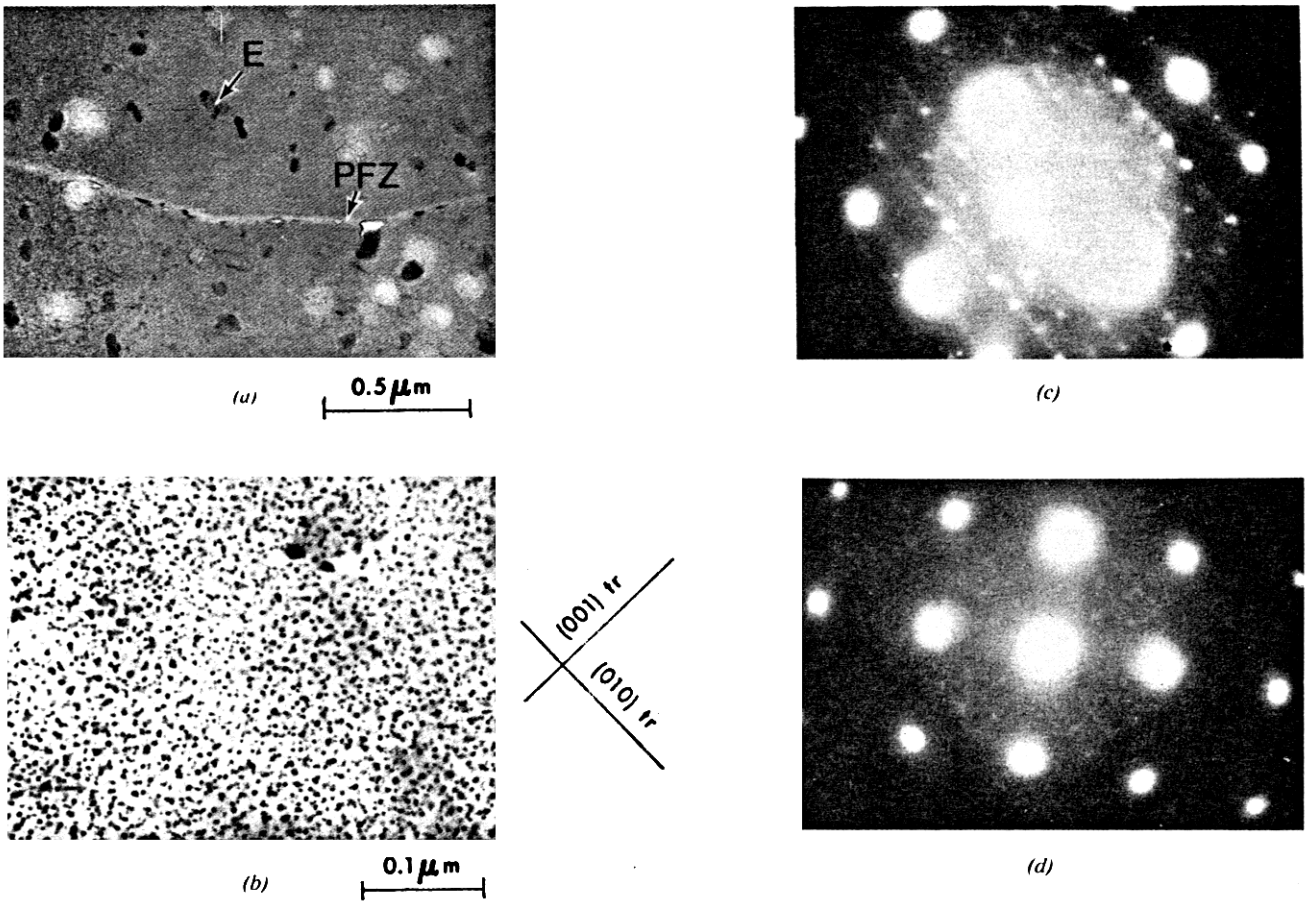

Fig. 8—(*a*) and (*b*) Typical multiple beam, bright field TEM micrographs exhibiting microstructural features representative of the compositions studied in the T6 temper. (*c*) and (*d*) (211) and (100) zone axes, respectively.

II lists the mean grain dimensions for all the alloys.

The unetched polished surfaces of these high purity alloys indicated that there were very few of the Fe and Si bearing constituents. Quantitative metallography showed a maximum of about 0.017 pct of these constituents. This is small enough not to contribute significantly to the final mechanical behavior on the basis of the results by Edelson and Baldwin.[22] All volume fraction data are listed in Table III.

Although pole figure data were not generated for these alloys, a cube texture (*i.e*, a (001) [100] texture with the [100] direction parallel to the rolling direction) has been observed for 7075 alloys with the same processing history.[23,24] Hence, it is likely that these alloys exhibit a similar preferred orientation. The ease of obtaining (100) zone axes diffraction patterns in the TEM, when the incident beam is normal to the rolling plane surface of the thin foils, supports this supposition.

Since all compositions were given identical processing and heat treatments and have comparable Mg/Zn ratios, the same general microstructural features were evident upon examination of thin foils in the transmission electron microscope (TEM). At intermediate magnifications (~50,000 times) the population of E-phase (incoherent Cr-bearing dispersoids) is visible throughout the matrix. In addition, narrow precipitate free zones of approximately 275Å in total width are evident along the grain boundaries (Fig. 8(*a*)). Table IV lists the PFZ width data for each alloy. From the superlattice reflections present in the selected area electron diffraction (SAED) patterns of all three alloys on the (100) and (211) zone axes, the microstructures were shown to consist of very fine, ordered Guinier-Preston (GP) zones and η' (Figs. 8(*b*) to (*d*)). The average size of these fine precipitates is approximately 40Å with a size spread varying between 20Å and 75Å.

To more clearly compare these microstructures,

Table V. TEM Quantitative Data for E-Phase Dispersoids*

Alloy	$\bar{d}_D$ (nm)	$\bar{\lambda}_D$ (nm)	$\bar{N}_v$ (in 10^{13} Particles/cm^3)	Vol Pct†
Low solute	79 ± 37	189 ± 12	2.57 ± 0.46	0.663
Intermediate solute	83 ± 58	200 ± 16	2.19 ± 0.50	0.656
High solute	81 ± 42	198 ± 13	2.26 ± 0.57	0.629

* Data indicate the mean ± one standard deviation.
† Calculated using the mean values for $\bar{d}_D$ and $\bar{N}_v$.

Table VI. TEM Quantitative Data for Grain Boundary Precipitates*

Alloy	$\bar{d}_p$ (nm)	$\bar{\lambda}_p$ (nm)	$\bar{N}_A$ (Precipitates/μm^2)	Areal Pct, f_p†
Low solute	20 ± 2	25 ± 2	392 ± 40	14
Intermediate solute	24 ± 1	27 ± 3	336 ± 51	15
High solute	25 ± 2	26 ± 3	357 ± 43	18

* Data indicate mean ± one standard deviation.
† Calculated using the mean values for $\bar{d}_p$ and $\bar{N}_A$.

quantitative transmission electron microscopy was performed to determine the average interparticle spacings, $\bar{\lambda}_D$, average diameters, $\bar{d}_D$, and numbers per unit volume, $\bar{N}_v$, of the E-phase dispersoid. The results of this study are tabulated in Table V. The three alloys exhibited similar results. The dispersoids were approximately 81 nm in diam, have an interparticle spacing of 196 nm, and have a population of 2.34×10^{13} dispersoids/cm^3. A Duncan multiple range test[25] for multiple comparisons showed that the three alloys were identical to each other with respect to $\bar{\lambda}_D$ and $\bar{d}_D$ with over a 95 pct confidence level. Similarly, the $\bar{N}_v$ values are comparable with a 90 pct confidence level. In addition, the volume fraction of these dispersoids was estimated. These calculations used the average values of $\bar{d}_D$ and $\bar{N}_v$ to obtain approximately 0.65 vol pct of dispersoids.

To more fully characterize the grain boundaries beyond the precipitate free zone width determinations, the grain boundary precipitate average diameter, $\bar{d}_p$, average intraplanar spacing, $\bar{\lambda}_p$, and average number per unit area, $\bar{N}_A$, were calculated. This data is presented in Table VI. The alloys, on the average, have grain boundary precipitates with an intraplanar particle spacing of 26 nm. They are 23 nm in diam, and have a population density of 362 precipitates/μm^2. There is evidence of a very slight increase in areal fraction of grain boundary precipitate with an increase in solute content. However, this difference is so minor that the areal fractions of grain boundary precipitates were regarded as equal at about 16 areal pct.

These alloys were tested in uniaxial tension to document the yield strength increase in the T6 temper by increasing the amount of solute addition. Data of σ_{ys}, σ_{UTS}, σ_f, ϵ_u, ϵ_f, and percent elongation (in a 25.4 mm gage length) are presented in Table VII. Flow curve parameters were determined for both curve fit forms:

$$\sigma = K_1 \epsilon_{pl}^{n_1} \quad [8]$$

and

$$\sigma = \sigma_o + K_2 \epsilon_{pl}^{n_2} \quad [9]$$

Therefore in Table VII, flow curve data with a one subscript refer to the first equation and those with a two subscript refer to the latter flow curve form. A better fit to the data is obtained using the second relationship. However, most data in the literature exist in the form of the first equation (Eq. [8]).

The quantitative microstructural characterization conducted demonstrates that these three alloys are identical in grain size and shape, dispersoid and grain boundary precipitate populations, and precipitate free zone widths. Since all three alloys yielded identical electron diffraction patterns, the matrix microstructures are identical and consist of ordered GP zones and η' which were measured to be of comparable size. However, the volume fraction of matrix precipitates would be expected to increase with increases in solute content for the same heat treatment. This is implied by the yield strength increase experienced as the solute content is increased. Therefore the tendency toward coarser slip with higher solute content must be related to the larger volume fraction of strengthening precipitate since all other parameters are identical. The implication is that the mechanism (in this case volume fraction of strengthening precipitate) used to increase one property (strength) may cause a decrease in another important property (toughness[8,18]) as slip behavior is altered. The differences in slip behavior can be explained by the following discussion.

In a precipitation hardening alloy that has small, coherent or semicoherent precipitates which are below

Table VII. Mechanical Properties

Alloy	σ_{ys} 0.2 Pct Yield Strength (MPa)*	Ultimate Tensile Strength (MPa)*	True Fracture Stress (MPa)*	Uniform Elongation ϵ_u	Tensile Fracture Strain ϵ_f	Pct Elongation (in 25.4 mm Gage Length)	K_1 (MPa)*†	n_1†	σ_o (MPa)*‡	K_2 (MPa)*‡	n_2‡
Low solute	496 ± 0.7	551 ± 2.1	672 ± 9.7	0.123 ± 0.006	0.278 ± 0.020	16.23 ± 0.17	718	0.070	490	549	0.680
Intermediate solute	583 ± 2.8	627 ± 2.1	773 ± 9.7	0.114 ± 0.001	0.247 ± 0.017	15.10 ± 0.35	790	0.058	576	518	0.657
High solute	602 ± 1.4	643 ± 1.4	771 ± 7.6	0.097 ± 0.007	0.210 ± 0.013	14.10 ± 0.67	802	0.054	595	496	0.639

Data indicate the mean ± one standard deviation where applicable.
* 1 ksi = 6.9 MPa.
† Flow curve parameters for the form $\sigma = K_1 \epsilon^{n1}$.
‡ Flow curve parameters for the form $\sigma = \sigma_o + K_1 \epsilon^{n2}$.

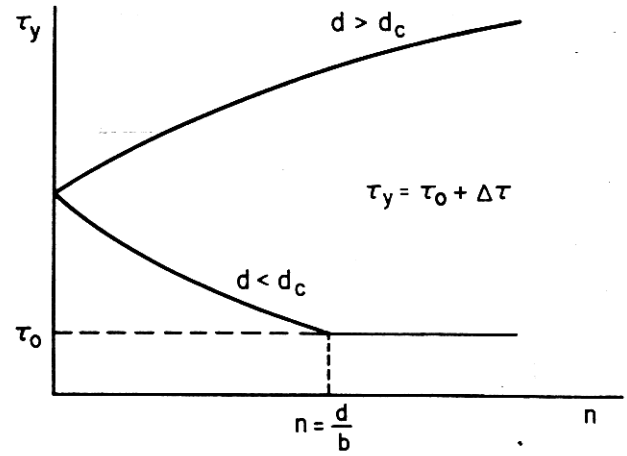

Fig. 9—Local critical shear stress as a function of the number of dislocations that have passed a slip plane ($d > d_c$: local work hardening; $d < d_c$: local work softening; n = number of dislocations; d = particle diameter, $\mathbf{b}$ = Burgers vector (Ref. 6).

the critical diameter (d_c) for dislocation bypassing to occur, the dislocations cut through these precipitates.[26,27] This leads to a softening of the slip band since each dislocation passing through these precipitates reduces the shear resisting cross section of the particle. The stress concentrations produced by an array of dislocations cutting through a series of precipitates quickly lead to a nonhardening steady state as calculated by Rau and Cook.[28] For the case where the diameters are larger than d_c, the dislocations can bow out between precipitates and lead to subsequent dislocation multiplication within that plane. This leads to local work hardening and promotes a homogeneous distribution of strain. Both cases are schematically shown in Fig. 9 where the local critical shear stress is plotted as a function of the number of dislocations (n) that have passed on a slip plane. Klein[29] and Hornbogen and Gahr[6] have demonstrated the connection between precipitate cutting and the formation of coarse slip bands. The model of Hornbogen and Gahr[6] will be presented briefly since this predicts the coarser slip of the high solute alloy relative to the low solute.

Hornbogen and Gahr[6] presented their model for the case of coherent, ordered precipitates that are small enough to be sheared. On the basis of another model by Gleiter and Hornbogen,[30] which considered the interaction of one flexible dislocation with the strengthening precipitates, the increase in yield stress, $\Delta\tau$, was given by

$$\Delta\tau(0) = \frac{\gamma_{APB}^{3/2} f^{1/3}}{G^{1/2}\mathbf{b}^2} d^{1/2}. \qquad [10]$$

$\Delta\tau(0)$ is the critical shear stress before passage of any dislocation; γ_{APB} is the antiphase boundary energy; f is the volume fraction of strengthening precipitate; and d is the precipitate diameter. G and $\mathbf{b}$ are the shear modulus and dislocation Burgers vector, respectively. The precipitate diameter can be written in terms of multiples of the Burgers vector as $d = n\mathbf{b}$. When n dislocations have passed in a plane through a precipitate, it is then completely sheared off and $\Delta\tau = 0$. The dependence of $\Delta\tau$ on n, *i.e.*, $\Delta\tau(n)$ depends on the shape, size distribution, volume fraction, and properties of the strengthening precipitate. Hence Hornbogen and Gahr[6] assumed a simplified calculation for cube-shaped, ordered, coherent precipitates interacting with a straight dislocation line as presented by Kelly and Nicholson:[31]

$$\Delta\tau(0) = \frac{\sqrt{3}}{4} \frac{\gamma_{APB}}{\mathbf{b}D} d \qquad [11]$$

where D is the interparticle spacing.

For the case where the ordered precipitates are sheared on {111} planes, the effective diameter, d, decreases linearly with the number of dislocations cutting them. The local critical shear stress increase is given by:

$$\Delta\tau(n) = \frac{\sqrt{3}}{4} \frac{\gamma_{APB}}{\mathbf{b}D} d \left(1 - \frac{n\mathbf{b}}{d}\right) \qquad [12]$$

The more the $\Delta\tau$ decreases with the passage of one dislocation, the greater will be the tendency towards inhomogeneous slip. Therefore, $d\tau/dn$ becomes a relative measure of the tendency for coarser slip due to work softening.

This is given by:

$$\frac{d\Delta\tau}{dn} = \frac{-\sqrt{3}}{4} \frac{\gamma_{APB}}{D} \qquad [13]$$

Since the interparticle spacing can be related to the precipitate diameter and volume fraction, a general equation of the following form is obtained where C is a geometrical constant:

$$\frac{\partial\Delta\tau(n)}{\partial n} = -C \frac{\gamma_{APB}}{d} f^{1/3} \qquad [14]$$

This equation indicates that increasing the volume fraction, f, or decreasing the diameter of the strengthening precipitate, d, results in a greater tendency for coarse slip. Hornbogen and Gahr[6] used Eq. [14] to predict the differences in slip behavior of an Fe-Ni-Al alloy exhibiting four characteristically different microstructures.

From this model of Hornbogen and Gahr, the tendency toward coarser slip can be predicted for the higher solute alloys since the volume fractions of the strengthening precipitate are greater in the higher solute alloys for the same diameter, d. A pseudo-binary phase diagram was assumed for the Al-$MgZn_2$ system from the ternary Al-Mg-Zn diagram to estimate the volume fractions of precipitate for the low and high solute alloys. This yields approximately a 20 pct larger value of $\partial\Delta\tau[n]/\partial n$ for the high solute. Hence, this implies that for the same macroscopic strain, there will be more strain localization within a given slip band for the high solute alloy. This could facilitate void nucleation at the grain boundaries at earlier macroscopic strains in the higher solute alloys. Subsequent research[8,18] has shown that the loss of fracture toughness with increasing solute content, for the T6 temper, can be related to this earlier fracture initiation at grain boundary-slip band intersections.

CONCLUSIONS

1) For $\epsilon_p = 0.02$, slip band spacings and slip step heights increase with increasing solute content, *i.e.*,

strain localization increases with solute content.

2) Extensive quantitative analysis has shown that the three high-purity 7XXX series aluminum alloys evaluated in this study differ only in the volume fraction of strengthening precipitate (ordered GP zones and η'). They are microstructurally identical in every other way for the T6 temper condition studied.

3) The tendency toward strain localization can be explained by a work softening model of Hornbogen and Gahr.[6] This model indicates that increasing the volume fraction or decreasing the diameter of the strengthening precipitate results in a greater tendency for coarse slip. For these alloys the volume fraction was the variable parameter with higher values corresponding with higher solute levels.

4) For those properties which are slip behavior dependent, such as macroscopic ductility and toughness, significant differences will be anticipated. Strain-to-fracture data from this study support this observation. This loss of ductility with increasing solute content has been observed before.[7]

5) The mechanism implemented to increase yield strength, which was increasing the volume fraction of strengthening precipitates, produced an increase in strain localization susceptibility. Applications of such a strengthening mechanism to alloy development must be carefully selected since other equally important properties may be diminished.

ACKNOWLEDGMENTS

The authors express their sincere appreciation to Dr. J. R. Low, Jr. who initiated this research program and provided valuable guidance until his retirement in August 1977. The authors also wish to thank Dr. H. Y. Hunsicker and Mr. J. T. Staley of the Alcoa Technical Center for their assistance. It was under their direction that the difficult task of producing high purity alloys was accomplished successfully. Dr. R. J. Rioja is gratefully acknowledged for his expert assistance in identifying the ordered GP zones. In addition, the sponsorship and financial assistance of the National Science Foundation at Washington, DC under NSF Grant DMR 76-02244 is acknowledged and duly appreciated, as is support from the Materials Research Laboratory Section of NSF through the use of central facilities.

REFERENCES

1. A. Gysler, S. Lutjering, and V. Gerold: *Acta Metall.*, 1974, vol. 22, p. 901.
2. G. Lutjering and S. Weissman: *Acta Metall*, 1970, vol. 18, p. 785.
3. M. J. Blackburn, and J. C. Williams: *ASM Trans. Q.*, 1969, vol. 62, p. 398.
4. R. J. Price and A. Kelly: *Acta Metall.*, 1964, vol. 12, p. 979.
5. J. D. Evensen, N. Ryum, and J. D. Embury: *Mater. Sci. Eng.*, 1975, vol. 18, p. 221.
6. E. Hornbogen and K. H. zum Gahr: *Metallography*, 1975, vol. 8, p. 181.
7. J. A. Nock and H. Y. Hunsicker: *J. Met.*, 1963, vol. 15, no. 3, p. 216.
8. G. M. Ludtka and D. E. Laughlin: Unpublished Research, Carnegie-Mellon University, Pittsburgh, PA, 1978.
9. G. L. Kehl: *The Principles of Metallographic Laboratory Practice*, p. 424, McGraw-Hill, New York, 1949.
10. J. E. Hilliard: *Quantitative Microscopy*, R. T. DeHoff and F. N. Rhines, eds., p. 45, McGraw Hill, New York, 1968.
11. F. Schuckher: *Quantitative Microscopy*, R. T. DeHoff and F. N. Rhines, eds., p. 201, McGraw-Hill, New York, 1968.
12. R. D. Schoone and E. A. Fischione: *Rev. Sci. Instruments*, 1966, vol. 37, p. 1351
13. J. Gurland: *Quantitative Microscopy*, R. T. DeHoff and F. N. Rhines, eds., p. 279, McGraw-Hill, New York, 1968.
14. J. W. Cahn and J. Nutting: *Trans. ASME*, 1959, vol. 215, p. 526.
15. J. W. Edington: *Practical Electron Microscopy in Materials Science*, p. 207, Van Nostrand Reinhold Company, London, 1976.
16. P. Hirsch, A. Howie, R. B. Nicholson, D. W. Pashley, and M. J. Whelan: *Electron Microscopy of Thin Crystals*, p. 420, Robert E. Krieger Publishing Co., Huntington, NY, 1977.
17. J. F. Mankivell: *B. J. Appl. Phys.*, 1963, vol. 13, p. 126.
18. G. M. Ludtka: Ph.D. Thesis, Carnegie-Mellon University, 1978.
19. C. R. Shastry and G. Judd: *Metall. Trans.*, 1971, vol. 2, p. 3283.
20. ASTM-E8-69, *Annual Book of ASTM Standards*, 1969, vol. 31, p. 196
21. J. A. O'Malia and B. F. Peters: *J. Mater.*, 1972, vol. 7, p. 510.
22. B. S. Edelson and W. M. Baldwin, Jr.: *Trans. ASM*, 1962, vol. 55, p. 230.
23. W. A. Anderson: *Aluminum*, K. R. VanHorn, ed., vol. 1, p. 99, ASM, Metals Park, OH, 1967.
24. T. H. Sanders, Jr.: Ph.D. Thesis, Department of Chemical Engineering, Georgia Institute of Technology, 1974.
25. I. Miller and J. E. Freund: *Probability and Statistics for Engineers*, p. 352, Printice-Hall, Inc., NJ, 1977.
26. H. A. Holl: *Corrosion*, 1967, vol. 23, p. 113.
27. N. Ryum: *Acta Met.*, 1968, vol. 16, p. 327.
28. C. A. Rau and T. S. Cook: Pratt and Whitney Aircraft Report 5868, p. 1, 1973.
29. H. P. Kein: *Z. Metallkd*, 1970, vol. 61, p. 564.
30. H. Gleiter and E. Hornbogen: *Phys. Status Solidi*, 1965, vol. 12, p. 235.
31. A. Kelly and R. B. Nicholson: *Prog. Mater. Sci.*, 1963, vol. 10, p. 217.